



Global estimates of seafloor slope from single-beam ship soundings

Joseph J. Becker¹ and David T. Sandwell¹

Received 13 August 2006; revised 7 January 2008; accepted 28 February 2008; published 30 May 2008.

[1] Rough topography on the ocean floor is a source of ocean mixing which is of interest to both physical oceanography and climate science. Most mixing has been attributed to high slopes of the large-scale structures of the deep ocean floor such as seamounts, continental margins, and mid-ocean ridge axes. In this paper, we show the small-scale but ubiquitous abyssal hills and fracture zones dominate the global map of rough topography. Much of this rugged seafloor occurs in the Southern Ocean on the flanks of the Pacific-Antarctic Rise and Southwest Indian Ridge. We present our results as a global map of the mean slope of the ocean floor, and as a global map of the ocean floor above the M_2 critical slope. We compare our results to multibeam and satellite bathymetry data to show that satellite bathymetry is not a valid proxy for multibeam measurements, but edited single-beam sonar data are adequate to provide a global perspective on features with horizontal wavelengths as small as 2 km.

Citation: Becker, J. J., and D. T. Sandwell (2008), Global estimates of seafloor slope from single-beam ship soundings, *J. Geophys. Res.*, 113, C05028, doi:10.1029/2006JC003879.

1. Introduction

[2] In a classic paper, *Munk* [1966] assumed constant upwelling and estimated the eddy diffusivity needed to maintain the observed abyssal ocean stratification as well as the amount of energy needed to mix the abyssal ocean. The $O(10^{-4} \text{ m}^2/\text{sec})$ diffusivity [*Munk*, 1966] predicted was not found experimentally [c.f. *Osborn*, 1980]. Eddy diffusivity is difficult to measure, but with the semiempirical methods of *Osborn* [1980; *Osborn and Cox*, 1972] and *Dillon* [1982], reliable experimental results were obtained. Recent measurements show that mixing is enhanced by orders of magnitude near rough topography [*Nash et al.*, 2007; *Polzin et al.*, 1997; *Toole et al.*, 1997]. *Munk and Wunsch* [1998] addressed the missing diffusivity in the mid ocean and the increased mixing over rough topography by proposing that tidal dissipation was a power source of mixing and mixing preferentially occurred when internal tides flowed across steep slopes. There is an extensive body of experimental, theoretical, and numerical research on the production of internal waves by the interaction of tidal currents with variable topography [cf. *Garrett and Kunze*, 2007]. *Baines* [1982] examined the simple case of horizontal tidal excursions impinging on a uniform continental slope and found that for semidiurnal tides in a stably stratified layer, there is a critical slope where conversion of the barotropic tide is most efficient. In the deep ocean where the stratification is low, this critical slope

ranges from 0.1 to 0.3 m/m so only very steep topography can generate internal waves in this simplified model. *Llewellyn Smith and Young* [2002] extended the model to show the shape of the topographic spectrum determines the amount of energy conversion in an ocean of finite depth with arbitrary stratification.

[3] Satellite altimetry has been used to measure the global barotropic tide [*Kantha*, 1995], as well as the location and magnitude of its global dissipation [*Egbert and Ray*, 2000, 2001, 2003]. The global dissipation studies indicated that the approximately 1/3 of the semidiurnal barotropic tidal dissipation occurs in the deep oceans, apparently over the mid-ocean ridges (MOR) and seamounts. However, the dissipation maps do not have sufficient spatial resolution to provide a clear correlation with seafloor structures [*Egbert and Ray*, 2003]. The lack of resolution reflects the wide track spacing of TOPEX/POSEIDON altimeter profiles (~ 150 km) as well as the subtlety and difficulty of the measurements presented by *Egbert and Ray* [2003].

[4] In this paper, we present the global spatial distribution of seafloor slope and roughness in the abyss (depth >2000 m). In particular, we focus on abyssal hills and fracture zones that extend over large parts of the ocean basins, especially on the lightly sedimented flanks of the slower spreading ridges. If, as proposed by *Ledwell et al.* [2000], most of the tidal dissipation in the deep ocean occurs on abyssal hills, mapping their global distribution is important. We also show a significant fraction of seafloor (4.5%) has slope greater than the M_2 critical slope. Much of this super critical seafloor occurs in the Southern Ocean on the flanks of the Pacific-Antarctic Rise and Southwest Indian Ridge. These high-slope facets have either not been detected before, or have been grossly underestimated because satellite bathym-

¹Institute of Geophysics and Planetary Physics, Scripps Institution of Oceanography, La Jolla, California, USA.

etry [Smith and Sandwell, 1997] does not resolve features having horizontal scales less than 10 km.

2. Global Estimate of Critical Slope

[5] While we are considering a more complete spectral analysis of the sounding data, a great deal can be learned from a simple “critical slope” analysis. The internal tide literature [Baines, 1982] describes topography as being either super or sub critical. A well-known approximation for the critical slope of the topography is [Baines, 1982]

$$\alpha^2 \approx \tan^2(\theta_g) = \frac{(\omega^2 - f^2)}{(N^2 - \omega^2)}, \quad (1)$$

where θ_g is the angle between the group velocity vector and the horizon, ω is the frequency of internal wave (radian/sec) generated by the M_2 tide, f is the inertial frequency and N is the buoyancy frequency. For waves of given frequency (always M_2 in this paper) at given latitude the only unknown is the buoyancy frequency which depends on the density profile,

$$N^2 = \frac{-g}{\rho} \frac{\partial \rho}{\partial z} - \frac{g^2}{c^2} \approx \frac{-g}{\rho} \frac{\partial \rho_\theta}{\partial z} \quad (2)$$

where z is the vertical coordinate, c is the speed of sound, ρ is the in situ density, ρ_θ the potential density, and g is the acceleration of gravity (9.8 m/s^2) [Knauss, 1997].

[6] A detailed global density profile is unavailable. We calculate an approximate buoyancy frequency profile using the CSIRO MATLAB routines [Morgan and Pender, 2003] at every depth and location in the 1° World Ocean Atlas (WOA) [Conkright et al., 2007]. Noise in the WOA values of temperature and salinity made the calculated values of N^2 noisy and occasionally negative. To stabilize our estimate of N , we first removed negative values of N^2 and other obvious errors, and then followed St Laurent and Garrett [2002] by fitting N to an exponential function of depth.

$$\ln(N) = c_0 + c_1 z. \quad (3)$$

[7] For depths that exceed the maximum depth in the WOA, we simply assumed N changes only slightly at abyssal depths, and used the deepest WOA depth at that location rather than extrapolate a fit to very noisy data. The calculated critical slope has at least two significant sources of error. First, the value of N is based on the WOA and which is an empirical data set with the usual potential for random and systematic errors. Second, our N is an empirical fit to an exponential of depth [St. Laurent and Garrett, 2002]; the truth is substantially more complex. As a result, our critical slope calculation is a semiquantitative result.

[8] To test the accuracy of our critical slope calculation we compared it to CTD data from two WOCE cruises. Appendix 1 is a comparison of our fit to the WOA data and WOCE CTD data along a meridian at 150° W between Alaska and Antarctica. We find good agreement between the critical slope estimates from these two independent data sets suggesting that the WOA data is adequate for this global analysis.

[9] The global map of critical slope based on work by Conkright et al. [2007] is shown in Figure 1. The map extends only to $\pm 72^\circ$, so the M_2 turning latitudes at 75° are not visible. The latitudinal trend toward a critical slope of zero at those turning latitudes is apparent, as is the general decrease of N (increasing critical slope) with increasing depth. Low critical slope occurs on the shallow continental margins, the crests of seamounts such as the Hawaiian ridge, and along the mid-ocean ridges with depths between 2000 and 3000 m. There is a prominent asymmetry between the North and South Pacific, east-west asymmetries in the South Atlantic, across the equatorial East Pacific Rise, and across the Ninety-East Ridge in the Indian Ocean. This asymmetry is also seen in the WOCE CTD analysis provided in Appendix A.

3. Satellite Bathymetry Greatly Underestimates Seafloor Roughness

[10] The slope of the ocean floor depends on the length scale of interest since, for example, individual pillow basalts can have vertical sides. The critical slope theory assumes that the length scale of the topography is greater than the tidal excursions of ~ 200 m [Garrett and Kunze, 2007]. A typical single-beam echo sounder has a beam width of $\sim 15^\circ$ so in the deep ocean (4000 m) it insonifies a zone about 1000 m across. Higher resolution (~ 200 m) is possible with modern multibeam systems but much of that data is collected at transit velocities, which limits the resolution to several hundred meters.

[11] Three types of measurement systems are used to map the topography and roughness of the ocean floor. Single-beam echo sounders, widely used since the 1960s, provide profile of depth from thousands of research cruises (Figure 2). While coverage is widespread, there are gaps as large as 200 km by 200 km, especially in the Southern Ocean. Multibeam echo sounding, available on most large research vessels since the mid 1990s, map 5–20 km wide swaths of seafloor at a horizontal resolution that depends on the depth of the water; 200–500 m at 4 km depth depending on ship speed and swath width. Ideally, the world’s oceans should be exhaustively measured with multibeam bathymetry, but only a small percentage of the ocean floor has been so measured [Smith and Sandwell, 2004]. The third approach combines the sparse ship soundings with dense satellite-derived gravity anomalies to estimate depth and roughness [Gille et al., 2000; Smith and Sandwell, 1997]. Satellite bathymetry can only resolve features with wavelengths between 20 and 160 km and misses most, if not all, of the small-scale roughness associated with the abyssal hill fabric. While none of these three measurement systems provides global coverage at the scales of interest (2–200 km), we show that the along-track analysis of the single beam provides an acceptable compromise between coverage and resolution if abyssal hills are assumed to be smoothly varying in slope over distances greater than a few hundred kilometers [Goff, 1991].

[12] To assess the accuracy and resolution capabilities of each of the three systems, we compared multibeam, single-beam, and satellite bathymetry along the track of an error-free, but otherwise typical cruise near the Atlantis Transform Fault on the Mid Atlantic Ridge (Figure 3). The multibeam

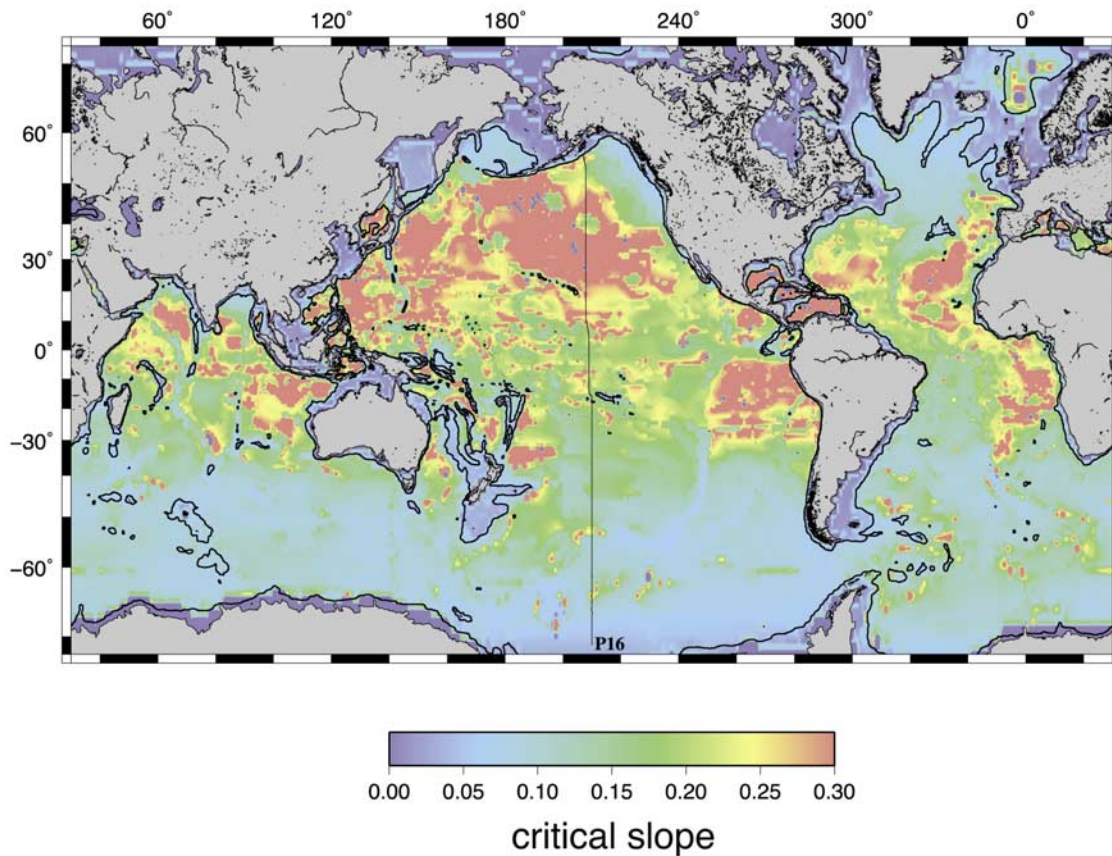


Figure 1. Critical slope derived from temperature and salinity data [Conkright *et al.*, 2007] interpolated and extrapolated to the bottom of the ocean. Black contour marks 3000 m depth. The WOCE P16 line along 150°W is also shown.

data are from a 500-m grid provided by the Ridge Multibeam Synthesis project [Carbotte *et al.*, 2004] and is considered in this paper to represent the “true” depth. The single-beam data were filtered and differentiated, as discussed below, to best match the multibeam slopes. Indeed the agreement between multibeam and single-beam data is quite good for both depth and slope. In contrast the satellite bathymetry does not capture the smaller-scale topography associated with the abyssal hills. This is evident in the slope comparison where the rms slope calculated from satellite bathymetry (0.038 m/m rms) is much smaller than the slope derived from the multibeam and single-beam systems (0.095 and 0.111 m/m rms). The inability of satellite bathymetry to accurately recover seafloor slope is illustrated in Figure 4, which shows a cumulative histogram of the absolute value of the slope for each of the three systems along the entire track line. Both sonar systems show that about 30% of the seafloor has slope greater than 0.1 m/m while the satellite bathymetry indicates only 2% of the seafloor of slope is greater than 0.1 m/m. This deficiency in the satellite bathymetry makes it unsuitable for quantifying seafloor slope due to abyssal hills.

[13] To further assess the accuracy and resolution of the single-beam data, we compared single-beam slopes of the 43 ship tracks in the Atlantis Fracture Zone area (Figure 2c) to slopes derived from a multibeam grid available at 200 m, 500 m, and 1500 m spacing. As noted above the footprint of a single-beam system in the deep ocean is ~ 1000 m but the

along-track sampling is only 330 m at transit speed so the true along-track resolution is probably somewhere between these two values. These grids were compiled by the Ridge Multibeam Synthesis Project [Carbotte *et al.*, 2004] and represent the best practices of the marine geology and geophysics community. It should be noted that there is a tradeoff between grid cell size and areal coverage so three resolutions are provided. While the 200-m resolution grids should provide the most accurate slope information, the coverage is much less complete than the 500-m grid. The 1500-m grid has the most complete coverage at the expense of lower resolution. To perform the slope comparison, the gradient of the multibeam grid was sampled along the trackline of the single-beam profile and the along-track slope was computed as the dot product of this gradient vector with the ship direction vector. The rms of the multibeam slope was 0.14, 0.12, and 0.10 m/m respectively, clearly showing a loss of roughness as the grid resolution increased from 200 m to 1500 m. In addition to rms, we performed a robust regression analysis between colocated single-beam profiles. A regression value greater than one indicates that the single-beam slope is overestimating the “true” seafloor slope or the multibeam grid is over-smoothed. The regression values for the 200-m and 500-m grids are close to one (1.04 and 1.09, respectively). In contrast, the slope of the single-beam data is 1.5 times greater than the slope derived from the 1500-m grid suggesting that the 1500-m grid is too smooth to fully

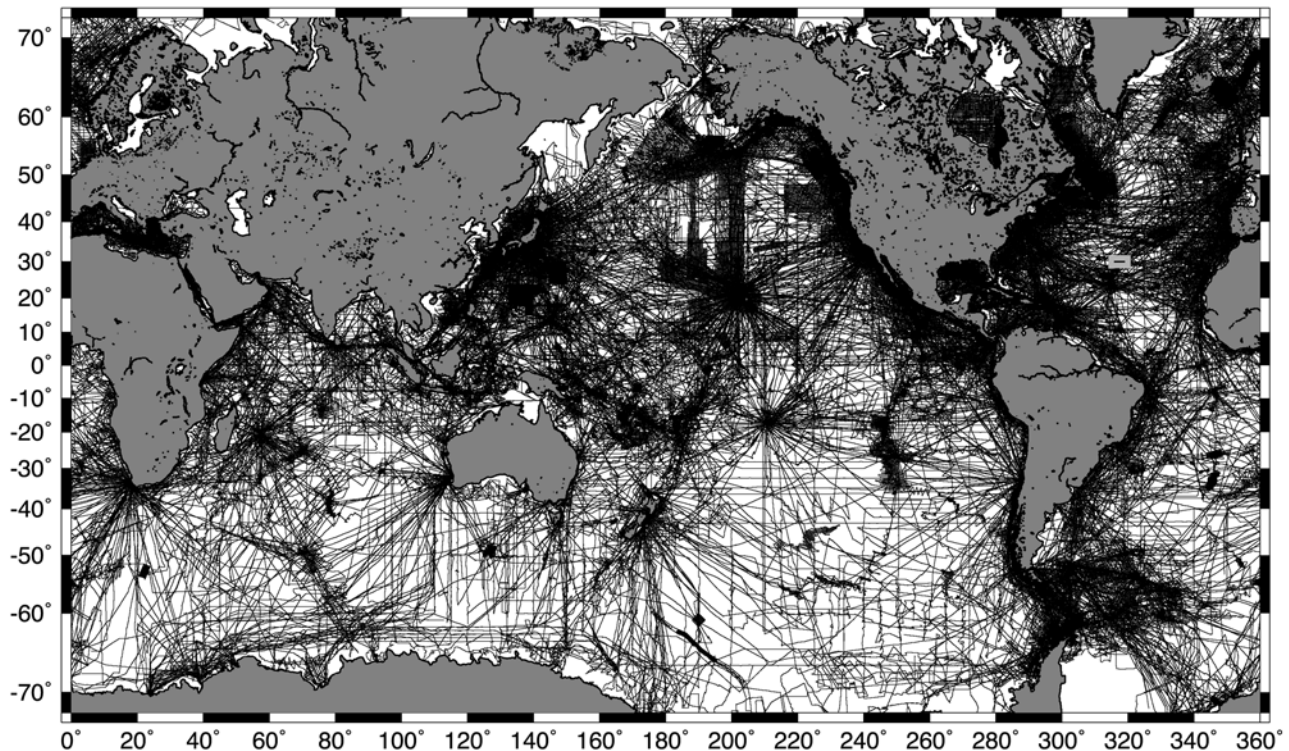


Figure 2a. Distribution of single-beam depth profiles from 4900 cruises collected over the past 40 years and archived at the National Geophysical Data Center. We have hand-edited these data to remove blunders and outliers.

capture seafloor slope at a wavelength of 2 km. These comparisons demonstrate that the along-track slope derived from a single-beam profile is similar in amplitude to the best multibeam grids at 200-m and 500-m resolution.

[14] While single-beam slope measurements are close to the multibeam “truth,” they have not been analyzed previously because the archived data are contaminated by many error sources. There are three main types of problems with the single-beam measurements. First, the depth soundings can be inaccurate owing to “blunders,” scale factor errors, and poor along-track sampling [Smith, 1993]. Second, older cruise data often contain large navigational errors that place soundings in the wrong location. While this is an issue for creating depth grids, navigation errors are not a problem for computing spatially averaged along-track slopes. Third, the coverage is nonuniform and the slope can only be computed along the track line of the ship. Track density is generally sparse in regions that are remote, have extreme weather, or are topographically uninteresting (Figure 2a). In particular the abyssal plains and hills, (far from ports, mid-ocean ridges and other areas of geologic interest), are poorly sampled. Since bathymetry derived from gravity data became available in 1997, cruises have often been planned to avoid areas of smooth topography. As a result, recent sounding data have a potential sampling bias toward rough seafloor that is difficult to quantify.

4. Method

[15] The most challenging issue related to the single-beam data is that slope can only be estimated along the track

line of each cruise leg. In lightly sedimented areas, seafloor fabric is dominated by abyssal hills (Figure 2c) that are elongated in the direction of the fossil spreading ridge, because they were formed by ridge-parallel normal faulting and volcanism [Goff, 1991; Goff and Smith, 2003; Macdonald and Luyendyk, 1985; Macdonald et al., 1996; Smith, 1998]. Because the abyssal hills have a preferred orientation, a single-beam profile must be oriented perpendicular to the hill to measure the full magnitude of the seafloor gradient. This is illustrated in Figure 5 where we have plotted the slope along the track line of many cruises against the magnitude of the gradient vector derived from a 500-m multibeam grid. Theoretically, the along-track slope should be less than the gradient, but in this example, there are deviations reflecting the inconsistencies in the two types of data due to the inherent smoothing of the measurement as well as the smoothing related to gridding.

[16] While the single-beam profiles measure only the along-track component of seafloor slope, their coverage is much more complete than the coverage of the multibeam swaths so they provide a better sampling of the global seafloor slope. We can partly overcome the 1-D sampling of a 2-D topography by projecting the statistical properties of the seafloor gradient to the statistical properties of along track slope. Appendix B provides an analysis that demonstrates the magnitude of the gradient of a patch of seafloor is typically $\pi/2$ higher than the along-track slope measured by a ship having a randomly oriented trackline. The orientation of the ship tracks, with respect to the abyssal fabric, is sometimes, but not always, random.

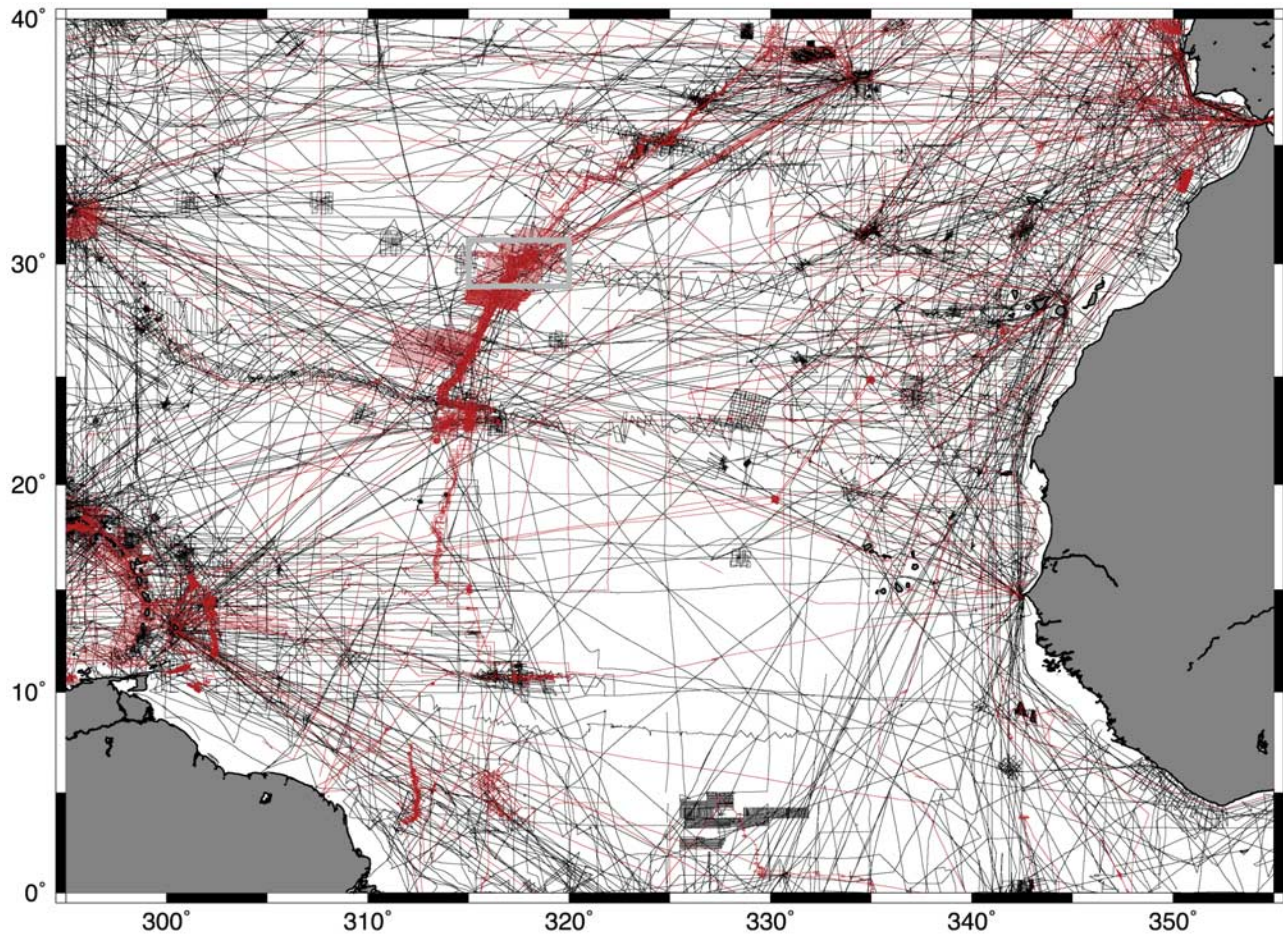


Figure 2b. Distribution of single-beam (black) and multibeam (red) echo soundings in the North Atlantic. Gray box shows area where single-beam, multibeam, and satellite bathymetry measurements were compared.

Seagoing expeditions not focused on seafloor geology, or cruises in transit across the basins, sample the abyssal fabric in an essentially random direction. However, a cruise focused on geology and geophysics is typically

preferentially oriented perpendicular or parallel to the abyssal fabric (e.g., Figure 2a, bottom). Because of this possible sampling direction bias, we report mean slope

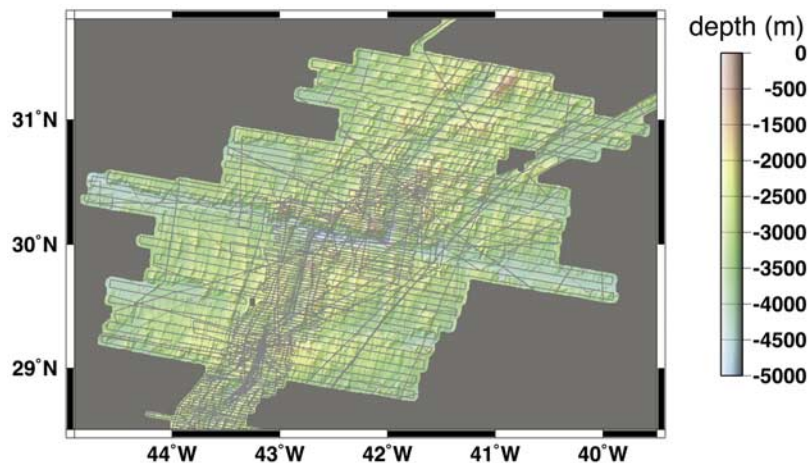


Figure 2c. Multibeam grid (500-m cell size) over the Mid-Atlantic Ridge and Atlantis Fracture Zone. Track lines are the single-beam or center-beam coverage used to relate 2-D gradients to 1-D slopes.

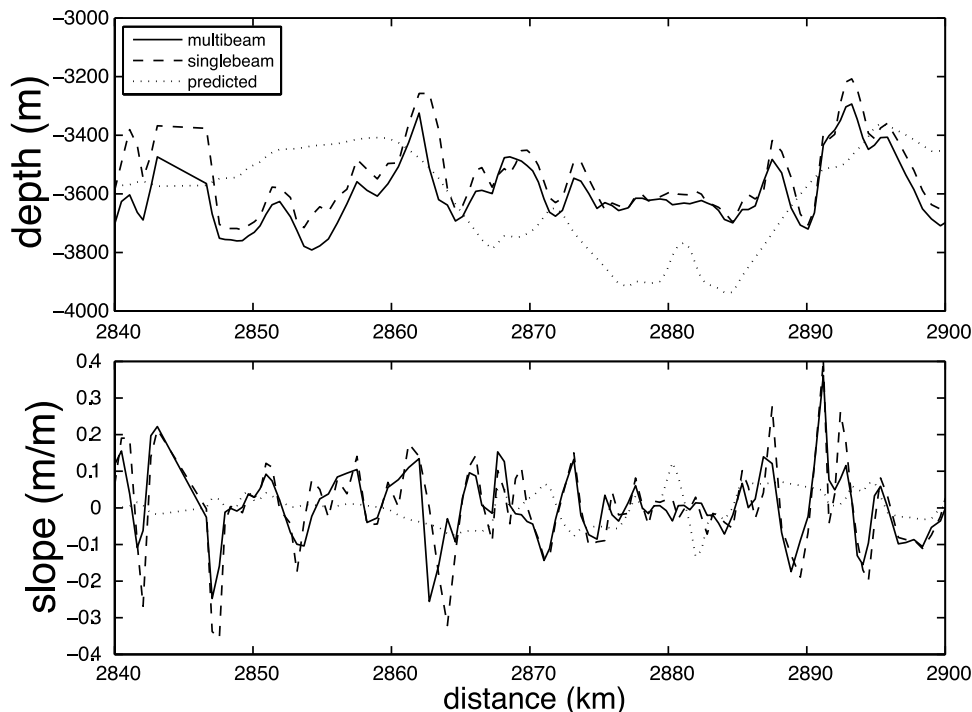


Figure 3. Seafloor (top) depth and (bottom) along-track slope along the trackline of a typical cruise near the Mid-Atlantic Ridge (MAR). Multibeam data were sampled from a grid having 500-m cell spacing and represent the “true” depth and slope. Single-beam data were filtered and processed along track to best match the multibeam profile. This version of satellite bathymetry was not forced to agree with available soundings so is representative of the accuracy in areas having no shipboard coverage. The rms differences are: single-beam depth 48.4 m, satellite bathymetry 190.8 m, single-beam slope 0.066 m/m, and multibeam slope 0.089 m/m.

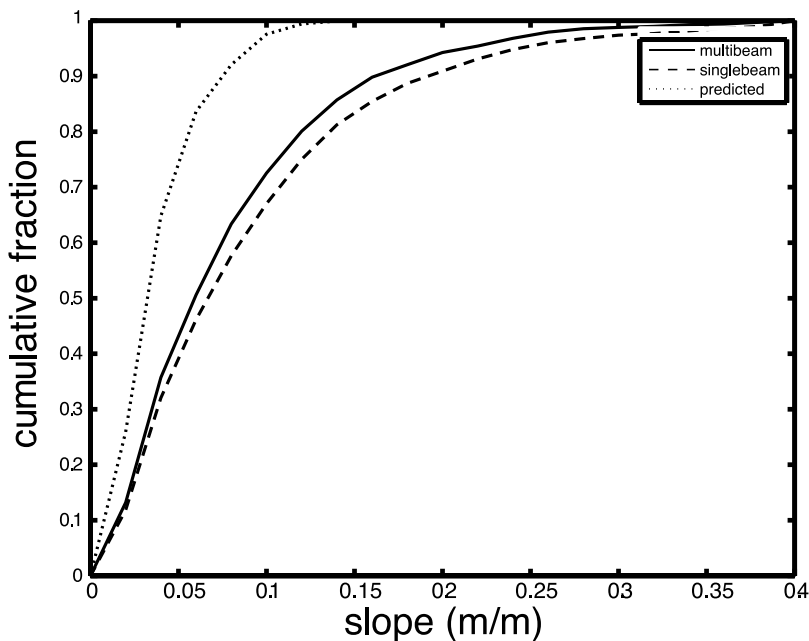


Figure 4. Cumulative histograms of the absolute value of the seafloor slope along the trackline from the three measurement systems. Thirty percent of the multibeam and single-beam slopes exceed 0.1 m/m, while only 2% of satellite bathymetry slopes exceeds 0.1 m/m.

without scaling up by $\pi/2$. This conservative approach understates the extent of supercritical seafloor.

5. Data Processing

[17] The examples provided so far have used single-beam data that are not contaminated by errors in depth or navigation. Approximately 1/3 of the 4900 cruise legs of single-beam bathymetry data available from the GEODAS database [National Geophysical Data Center, 2006] have significant errors. These 1800 cruises have never been used in the global satellite bathymetry maps [Smith and Sandwell, 1997] even though, in many cases, the entire month-long set of depth soundings had only a few outliers. The automatic algorithm used to screen out obviously bad cruises generally failed to identify the occasional bad pings in good cruises because the types of errors are so diverse. Typical errors include: navigation errors, digitizing errors, typographical errors due to hand entry of older sounding, reporting the data in fathoms instead of meters, incorrect sound speed measurements, and even computer errors in reading punch cards [Smith, 1993]. Just one bad section of a cruise in an isolated region introduces a seafloor topographic feature that does not exist and the entire cruise is rejected.

[18] About 5000 cruises of single-beam soundings collected over the past 40 years and archived at the National Geophysical Data Center [2006] have been hand edited by comparing measured depth to satellite bathymetry (i.e., based on gravity only). These data will be combined with multibeam data to refine the global satellite bathymetry grid [Smith and Sandwell, 1997] and create a new global grid at 1 km resolution. This involved the development of a graphical user interface program consisting of three linked windows, the ship track, the along track profile, and a scatter diagram of altimetric versus measured depth. Typical rms differences between the measured and satellite bathymetry are 250 m. We expect the rms errors in the soundings to be less than 25 m [Smith, 1993] so most of the bad soundings are obvious outliers. The analyst scans the profile data for large deviations from the satellite bathymetry (typically > 500 m) and flags these data as being suspect. The edited cruise is returned to the database with the suspect data flagged. Using this tool, we have edited the approximately 30 million pings from the GEODAS database.

[19] These clean data were then low-pass filtered and differentiated along track to estimate seafloor slope as discussed below using the software tools in GMT [Wessel and Smith, 1995]. The ship track profiles were prefiltered with a Gaussian low-pass filter having a 0.5 gain at a wavelength of 2 km. The 2-km filter is partly motivated by the expected beam width of single-beam sonar (~ 1 km) in the deep ocean (W. H. F. Smith, personal communication, 2005). Ship track data are unequally spaced; for example, the ship speed changes, but the ping rate is relatively uniform. Moreover, the spacing of the older hand-digitized data is based on the seafloor features. For example, flat abyssal plains sometimes have 4-km spacing between soundings because the human digitizer determined that a finer spacing was unnecessary. This uneven and sometimes large spacing does not strictly support a 2-km wavelength resolution. We selected this resolution as a compromise because the widely spaced older soundings presumably

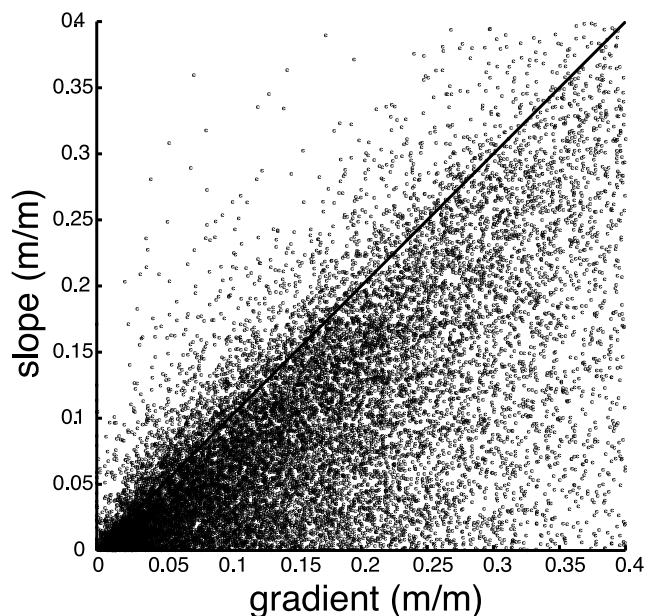


Figure 5. Magnitude of along-track slope of the seafloor from single-beam data (Figure 3, bottom) versus magnitude of gradient vector at the same locations from a 500-m multibeam grid. Theoretically the 1-D slope should be less than or equal to the 2-D gradient.

would have a smaller spacing if the human digitizer felt it was needed to capture the actual seafloor slope. After low-pass filtering, the data were differentiated along track at a minimum interval of 1/4 the wavelength of the low-pass filter (500 m). More complex signal processing is not needed when the ship track data is correctly edited.

[20] The calculation of the fraction of seafloor above critical slope discussed below was done in three steps in order to minimize the bias due to the uneven distribution of ship soundings. First, we created two 0.1° longitude by 0.1° latitude grids, one consisting of the total number of slope estimates in each grid cell and a second consisting of the number of slope estimates (absolute value) that exceed the critical slope in each grid cell. Second, these two grids were low-pass filtered with a radial Gaussian filter ($\sigma = 10$ km) to determine the number of slopes per 628 km^2 ; the integrated area under a radial Gaussian is $2\pi\sigma^2$. Third, the fraction of seafloor with slope above the critical slope was computed as the ratio of the two grids. Areas with less than one ping per 100 km^2 were not used to avoid taking the ratio of very small numbers. For display purposes, the fraction of seafloor above critical slope is median filtered and interpolated onto a 1° grid (Figure 7a). This process combines the information in Figures 6 and 7.

6. Global Measurement of Seafloor Roughness

[21] The global map of spatially averaged seafloor slope is shown in Figure 6. Along-track slopes were binned in a 0.25° longitude by 0.2° latitude intermediate grid and the mean slope was calculated for each bin. The binning is done to reduce the bias due to uneven sampling by the ship soundings. In particular, the ridge axes are sampled much more densely than the abyssal plains. We find that seafloor

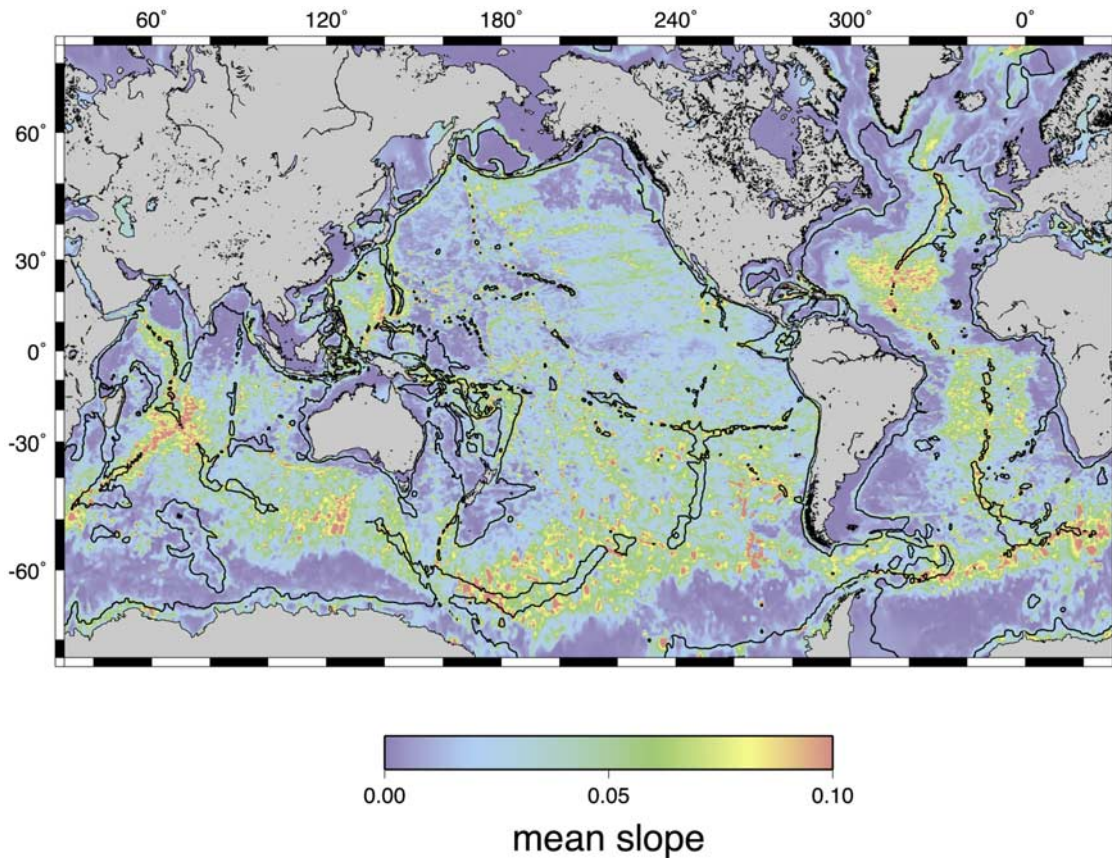


Figure 6. Mean slope of the seafloor filtered with a 60-km Gaussian filter and interpolated on a 0.5° grid. Contour line at 3000 m depth highlights the deep ocean basins and shows the ridges are not as steep. Mean slope commonly exceeds 0.05 m/m on the flanks of the seafloor spreading ridges, especially the ridges spreading at a rate of <70 mm/a.

slope varies more than an order of magnitude throughout the deep oceans and depends on a combination of tectonic and sedimentary processes. Large-scale features (>40 km) such as continental margins, ridge axes, fracture zones, trenches, and seamounts are sometimes associated with slope greater than 0.05. These large-scale features are well resolved in bathymetry derived from satellite-derived gravity anomalies and sparse ship soundings [Smith and Sandwell, 1997]. Such maps have been band-pass filtered between 20 and 160 km wavelength to reveal the slope and roughness of the seafloor and to relate these bottom characteristics to mesoscale variability [Gille *et al.*, 2000] and ocean mixing [Jayne and St Laurent, 2001].

[22] Using only ship soundings, we find that the global mean slope map is dominated by the distribution of the smaller-scale abyssal hill topography and fracture zones. Abyssal hills are generated at mid-ocean ridges by a combination of volcanism and normal faulting [Cannat *et al.*, 2006; Lonsdale, 1977; Macdonald and Luyendyk, 1985]. The amplitude and wavelength of abyssal hills depends strongly on the rate of seafloor spreading [Goff, 1991; Goff *et al.*, 2004; Kunze and Llewellyn Smith, 2004] that also controls the morphology of the spreading ridge axis where they were formed [Canuto *et al.*, 2004; Macdonald, 1982; Macdonald *et al.*, 1988; Menard, 1967; Small and Sandwell, 1992]. On older seafloor, a thick layer

of sediment often covers the abyssal fabric. Sedimented seafloor can be extremely flat at the scale of abyssal hills. In summary, there are basin-scale variations in seafloor slope that are well explained in terms of variations in seafloor spreading rate and the thickness of the sediments. These spatial variations in slope occur over distances greater than a few hundred kilometers [Goff and Jordan, 1989] so the sparse track sampling in the Southern Ocean (~ 40 km track spacing) is adequate for characterizing global seafloor slope.

7. Fraction of Seafloor Above Critical Slope

[23] Given the slope along each ship track and the critical slope interpolated to the same location we calculate the fraction of seafloor having slope above the critical slope. This calculation allows us to estimate the total area of super critical seafloor. It is also useful because it at least partially addresses the issue of mixing hot spots. [Nash *et al.*, 2007] suggest that mixing in the deep ocean is localized in a few small areas. Therefore, an area's potential for mixing may not be the average critical slope, but the fraction of the area that is super critical.

[24] For comparison, we performed a similar analysis using the global 2-min grid of Smith and Sandwell [1997] (Figure 7b). Since the full gradient of the Smith and

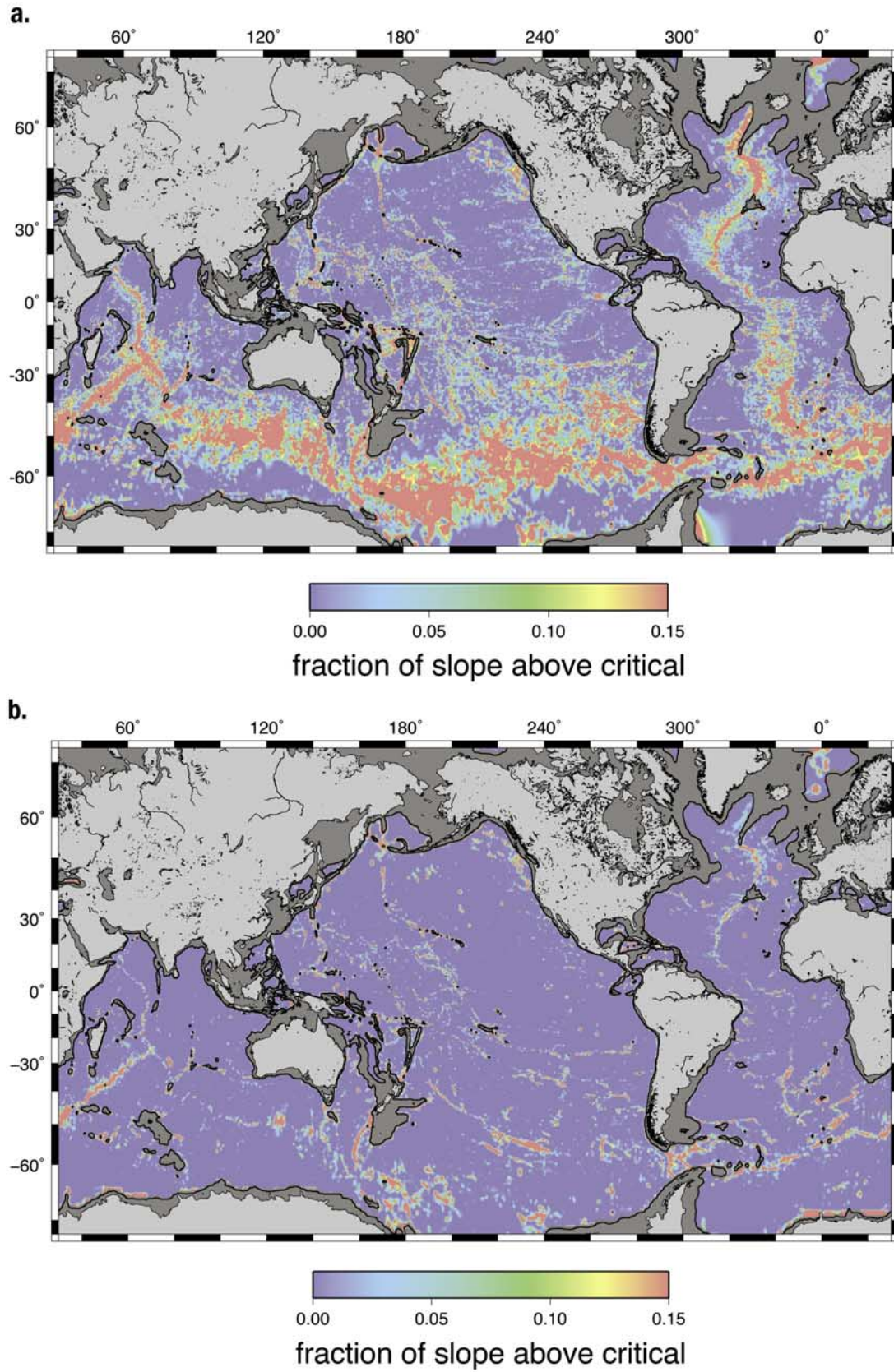


Figure 7. (a) Fraction of seafloor having slope exceeding the critical slope for depth > 2000 m. Fraction is derived from single-beam soundings. (b) Fraction of seafloor having slope exceeding the critical slope for depth > 2000 m. Fraction is derived from satellite bathymetry [Smith and Sandwell, 1997].

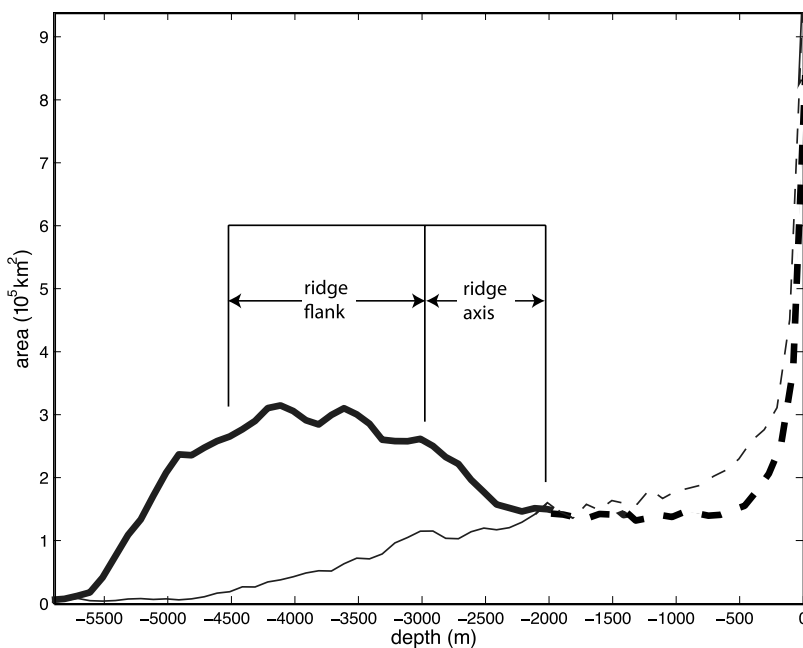


Figure 8. Area of seafloor with above critical slope as a function of depth. Thick curve is from single-beam data while the thin curve is from satellite bathymetry. Seafloor slopes from satellite bathymetry clearly underestimate supercritical area with depth < 2000 m. The critical slope calculation is unreliable for shallow depths < 2000 m.

Sandwell [1997] grid was calculated, we would expect slopes from the gradient of *Smith and Sandwell* [1997] to be $\pi/2$ times greater than single-beam slopes, and thus the fraction of seafloor above the critical slope should be $\pi/2$ larger. Instead, we find the supercritical fraction of seafloor for [*Smith and Sandwell*, 1997] to be substantially less than that derived from the single-beam soundings. This is because, as discussed above, satellite bathymetry does not capture the full magnitude of the seafloor gradient because it only resolves wavelengths > 20 km.

[25] The ship data and the satellite bathymetry grid have similar supercritical seafloor fraction for the large-scale structures of the ocean basins such as continental margins, ridge axes, ocean trenches and back-arc volcanoes and intraplate island chains such as Hawaii. This is expected because these large-scale features are well resolved in the satellite bathymetry grid. However, there are major differences (Figures 7a and 7b) on the flanks of ridges especially in the Southern Ocean where the critical slope at the bottom of the ocean is less than 0.2 m/m.

[26] To quantify this observation we plot the area of seafloor with supercritical slope versus ocean depth (Figure 8, thick line). Seafloor spreading ridges lie at depths between 2000 m and 3000 m. The ridge flanks lie at depths between 3000 m and 4500 m. It is clear that the fraction of supercritical seafloor on the ridge flanks is larger than the fraction of supercritical seafloor on the ridge axes. A similar analysis using satellite bathymetry arrives at just the opposite conclusion and suggests that the ridge axes are more important than the ridge flanks. Indeed the total fraction of supercritical seafloor in the deep ocean (>2000 m deep) is 4.5% based on the single-beam data and only 1.5% based on the satellite bathymetry. These comparisons suggests that calculations based on slopes of the [*Smith and Sandwell*,

1997] grid are substantially underestimating the area of super critical seafloor, and its location.

8. Discussion and Conclusions

[27] We restrict our discussion to the deeper ocean areas (>2000 m) where abyssal hills dominate the seafloor slope, and where we expect that spatial variations in slope and critical slope will be smooth relative to the characteristic spacing of the ship profiles. Our estimate of the fraction of seafloor above critical slope shows some obvious global patterns that deserve comment. The west flank of the southern Mid-Atlantic Ridge is prominent, but areas of rough seafloor in the Southern Ocean dominate the fraction of seafloor above critical. In particular, the flanks of the Southwest Indian Ridge and the flanks of the Southeast Indian Ridge, especially in the Australian-Antarctic Discordant Zone (90°E–160°E) are prominent as are the flanks of the Pacific-Antarctic Rise, and the flanks of the Scotia Sea Spreading Centers (50°S–60°S, 75°W–30°W). The presence of so much super critical topography near the Antarctic Circumpolar Current (ACC) is striking. We speculate that the ACC may be sweeping the sediment off the ridge flanks, creating an area of rough topography in a strong current.

[28] Our conclusions are as follows.

[29] 1. The 40-year archive of single-beam bathymetry provides a global perspective on the slope and roughness of the seafloor although the data have some significant shortcomings. First, the original data are highly heterogeneous because they were collected with multiple generations of echo sounding and navigation technology and were digitized and assembled by hundreds of scientists on tens of research vessels. By visually editing 4900 cruises assembled at NGDC, we were able to extract seafloor slope and

roughness information for wavelengths greater than 2 km and confirmed the results in small areas where complete multibeam coverage is available. A second problem with the single-beam bathymetry data is that the seafloor slope can only be estimated along the trackline of the ship, which is usually not in the direction of maximum seafloor gradient. Assuming the direction of the ship tracks is random with respect to the abyssal hill fabric, we show that, on average, the along-track slope will be $2/\pi$ less than the magnitude of the gradient. We use the along-track slope estimate as a proxy for seafloor slope knowing it represents a lower bound on the actual slope.

[30] 2. The critical slope at the bottom of the ocean associated with conversion of the barotropic M_2 tide was estimated from a global compilation of temperature and salinity measurements [Conkright *et al.*, 2007]. Sparse measurements, especially in the Southern Ocean, prevent the construction of a spatially detailed map of critical slope. We argue that in the deep ocean (<2000 m) spatial variations in temperature and salinity will be small so this global representation may be qualitatively correct. Interpolating this critical slope map to the locations of the measured seafloor slope, we estimate the fraction of seafloor with slope that exceeds the critical value. In contrast to previous studies based on altimetry-derived depth, we find large areas that have slope exceeding the critical value.

[31] 3. Our results are consistent with previous studies that show a high fraction of seafloor above critical slope along the Mid-Atlantic Ridge and Hawaiian Chain but suggest that barotropic tidal conversion dominantly occurs in the Southern Ocean where sediments are thin and the abyssal hills have relatively high amplitude because they formed at a fossil spreading rate less than the threshold value of 70 mm/a. The global analysis shows that the largest areas of supercritical slope are on the flanks of the seafloor spreading ridges. The largest areas of supercritical slope are the Southwest Indian Ridge flanks, the Southeast Indian Ridge flanks, the southern Mid-Atlantic Ridge flanks, the Scotia Ridge, and most importantly, the Pacific Antarctic Rise away from the ridge axis.

Appendix A: Comparison of Critical Slope From WOCE P16 CTD Casts and Numerical Fits to WOA 2001

[32] The global map of critical slope (Figure 1) shows obvious hemispherical variation with the lower critical slope in the South Pacific than North Pacific. To verify this hemispherical asymmetry, we compared our numerical fit of World Ocean Atlas (WOA) 2001 data [Conkright *et al.*, 2007] to the critical slope calculated from Salinity, Temperature, and Pressure data (commonly referred to as CTD) from two World Ocean Circulation Experiment (WOCE) repeat cruises in 2005/2006. These cruises revisited the “P16” line in the Pacific that runs along longitude 150°W from Antarctica to Alaska with a CTD cast taken at least once every degree of latitude from 72°S to 56°N. These particular data were not used in the WOA 2001 analysis [Conkright *et al.*, 2007]. The 2005/2006 cruises had modern navigation and CTD instrumentation and they sampled the entire water column from surface to approximately 10m above the bottom. A typical CTD rosette has redundant sensors that are

calibrated on shore and against each other on each station. The noise present in the data is on the order of 1 part per thousand or better. This level of instrument noise is inconsequential since the microstructure of the water column dominates the instrumentation noise. The standard deviation of N due to the microstructure was typically 0.25 cph in the deepest bin, which is a large fraction of the total estimate of N so this environmental noise dominates. At one station in the North Pacific at 28°N, either an overturn was observed at the bottom, or there was a data error large enough to create a negative N^2 . As in the cases of computing N from the WOA, this value of N and the critical slope are both set to zero.

[33] The CTD data from 190 casts were processed into critical slope at the bottom of the ocean as follows. The “exchange” data in comma separated value (CSV) format from the 2005 repeat of the P16S line on cruise 33RR200501, and the 2006 repeat of P16N from cruise 325020060213 were down loaded from the CLIVAR & Carbon Hydrography Office (CCHDO) website (J. Swift, <http://cchdo.ucsd.edu>, accessed 2 January 2008) and processed using MATLAB software [MathWorks, 2007]. For each of the depth casts, the CTD were processed using the CSIRO algorithm [Morgan and Pender, 2003] of the UNESCO seawater equation of state. The data for each cast were then binned and averaged at the WOA standard depths. The deepest bin in each P16 station was compared to the numerical fit from the WOA 2001 data [Conkright *et al.*, 2007]. The maximum depth of the water at P16 stations is rarely more than 100 m deeper than the maximum standard depth in the WOA.

[34] Estimates of critical slope from the WOA and P16 are plotted in Figure A1 and show good agreement. Both estimates have an unknown uncertainty that is dominated by true fluctuations in density gradient. Therefore we performed a robust regression [Laws, 1997] using a “bisquare” weighting function in the MATLAB robustfit function where the model was constrained to go through the origin. Our calculation of critical slope using the WOA is slightly smaller than the experimental data (0.958 ± 0.085), but it is within 5 percent of the experimental result and is consistent with a slope of one. The linear correlation is 0.497. The WOA data also show some anomalously high slopes that are due to underestimating the density gradient. Considering that the microstructure of N in the experimental data is approximately $\pm 50\%$, we feel our use of a fit to the WOA to estimate global critical slope is justified.

[35] Given this level of agreement we believe the north-south asymmetry in critical slope, shown in Figure 1, is real. Along this line of longitude the asymmetry is to be expected because of the Pacific basin in the northern hemisphere is generally 1–2 km deeper than the flank of the Pacific Antarctic Rise in the southern hemisphere and deeper ocean tends to be more stratified than shallower ocean. In conclusion, a critical slope calculated from WOA is error prone, but in good agreement with the more accurate CTD data.

Appendix B: Statistical Relationship Between Slope and Gradient

[36] Assume the abyssal seafloor away from isolated seamounts and other distinct features is a stationary and ergodic function [Bendat and Piersol, 2000]. The gradient

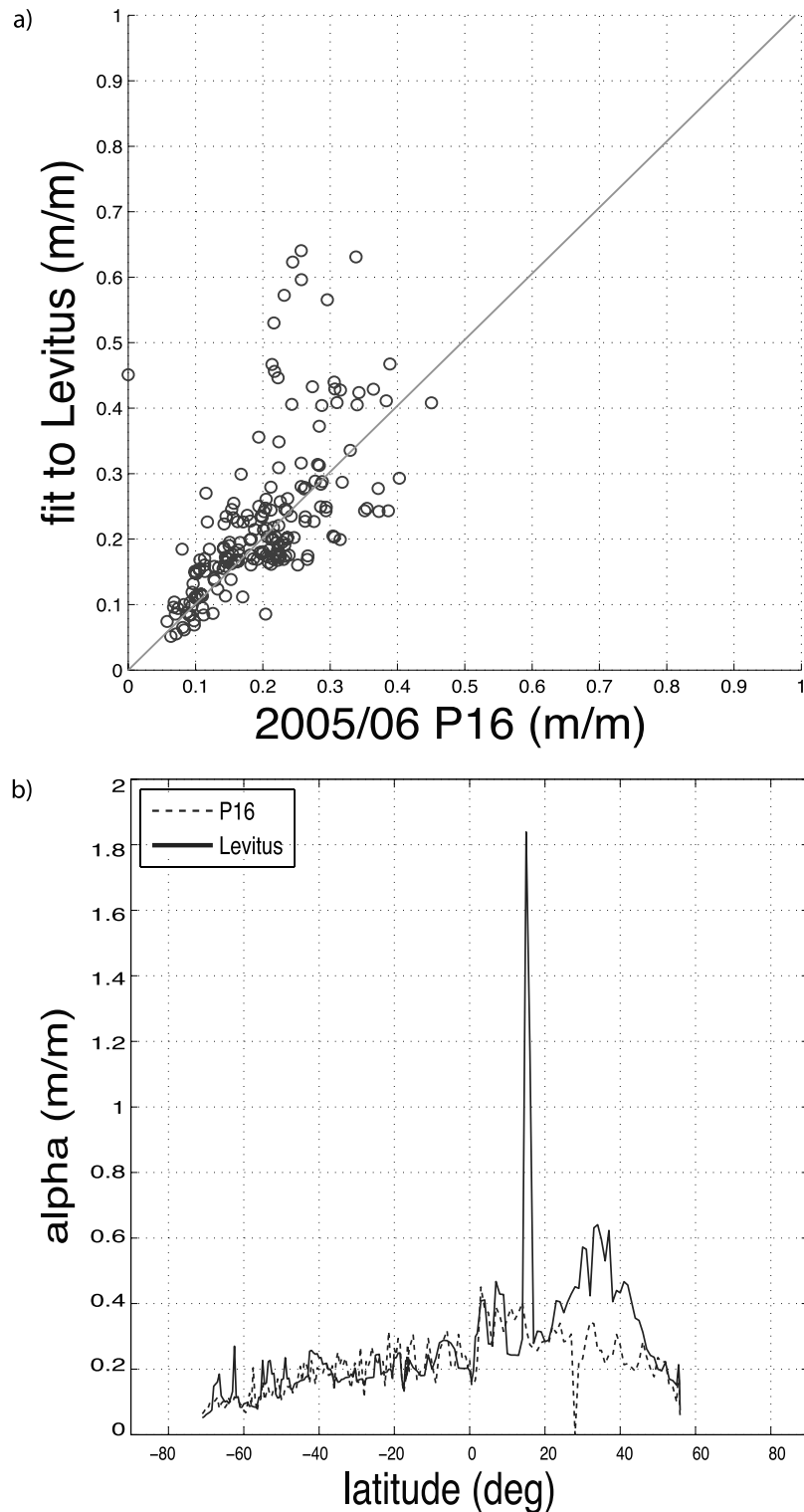


Figure A1. (a) Scatterplot of critical slope calculated from WOA and P16 cruise data. (b) Meridional plot of critical slope calculated from WOA and P16 cruise data.

of a randomly oriented facet of seafloor is a random vector [Goff, 1991]. Our objective is to describe the statistical properties of the gradient vector as well as to relate this to the statistical properties of the slope vector. Following Goff [1991], assume the x - and y -components of the gradient are independent, zero mean, and normally distributed with

identical variance σ^2 . As discussed by Freilich [1997], the histogram of the magnitude of this random vector is a Rayleigh distribution ($x > 0$)

$$f_{\text{Rayleigh}}(x; \sigma) = \frac{x}{\sigma^2} \exp\left(\frac{-x^2}{2\sigma^2}\right). \quad (\text{B1})$$

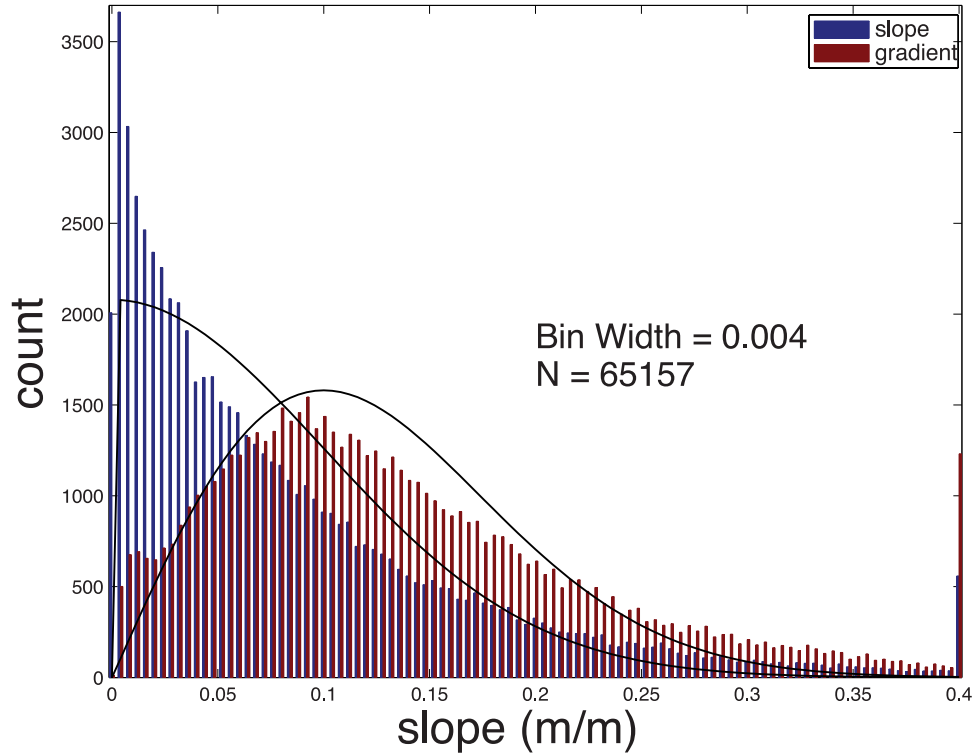


Figure B1. Histograms of the magnitude of the slope (blue) and gradient (red) for the data shown in Figure 5. The theoretical histogram for a Rayleigh distribution with a mean slope of 0.152 m/m provides an adequate fit to the actual gradient distribution. Mapping the gradient distribution into slope distribution provides an adequate fit to the actual slope distribution. The mean value of the theoretical slope distribution is $2/\pi$ times the mean value of the gradient distribution.

[37] The mean value of the gradient g is

$$\bar{g} = \int_{g=0}^{\infty} g \cdot f(g; \sigma) dg = \sigma \sqrt{\frac{\pi}{2}}. \quad (\text{B2})$$

[38] Given this statistical model for seafloor slope we can relate the probability distribution of along-track slope to the Rayleigh distribution of gradient. Consider a tilted facet of seafloor oriented at an azimuth of ϕ with respect to the track line of the ship. The measured slope of the seafloor is always less than or equal to the magnitude of the gradient and it is given by $s = g \cos \phi$. The distribution for along track slope is related to the probability distribution for gradient by

$$\begin{aligned} f(s; \phi, \sigma) &= f_{\text{Rayleigh}}(s / \cos \phi; \sigma) \left| \frac{\partial g}{\partial s} \right| \\ &= \frac{s}{\sigma^2 \cos^2 \phi} \exp\left(\frac{-s^2}{2\sigma^2 \cos^2 \phi}\right). \end{aligned} \quad (\text{B3})$$

[39] We need to integrate over all azimuths and normalize by 2π to obtain the distribution for a randomly oriented facet.

$$f(s; \sigma) = \frac{1}{2\pi} \int_0^{2\pi} f(s; \phi, \sigma) d\phi = \sqrt{\frac{2}{\pi\sigma^2}} \exp\left(\frac{-s^2}{2\sigma^2}\right). \quad (\text{B4})$$

[40] The Rayleigh distribution describing the gradient maps to a Gaussian distribution describing the along track

slope. An example of theoretical gradient and slope distribution functions are shown in Figure B1 along with the histograms of observed gradient and slope shown in Figure 5. While there are discrepancies between the actual and model distribution functions, these simple ideas provide an approximate basis for deriving seafloor gradient information from along-track slope profiles. In particular, it is interesting to relate the mean along track slope to the mean gradient, ($s > 0$)

$$\bar{s} = \int_0^{\infty} s \cdot f(s; \sigma) ds = \sigma \sqrt{\frac{2}{\pi}} = \frac{2}{\pi} \bar{g}. \quad (\text{B5})$$

[41] This relationship suggests the mean value of slope measured along a ship track is lower than the gradient by a factor of $2/\pi$ (64%). In this paper, we compute mean slope along ship tracks, and expect that the seafloor gradient is usually larger.

[42] **Acknowledgments.** This paper benefited greatly from discussions with Walter Munk, Stefan Llewellyn Smith, Shaun Johnston, Sarah Gille, and Jennifer MacKinnon. Scott Nelson of UCSD edited the ship data with an astonishing rapidity and accuracy. We thank the Associate Editor James Richman and the two reviewers for their many suggestions for improving the manuscript. We also thank Walter Munk for originally proposing this study in 1999 using satellite bathymetry. That preliminary comparison suggested (incorrectly) that the abyssal plains were not important in deep ocean mixing. The results were not published because we speculated that the slope of the seafloor from satellite bathymetry greatly underestimates the true seafloor slope. It has taken 8 years to go back, look

at the raw sounding data, and arrive at a more accurate assessment. This research was supported by the Office of Naval Research (N00014-06-1-0140) and the National Science Foundation (OCE-0326707).

References

- Baines, P. G. (1982), On internal tide generation models, *Deep Sea Res., Part I*, 29, 307–338, doi:10.1016/0198-0149(82)90098-X.
- Bendat, J. S., and A. G. Piersol (2000), *Measurement and Analysis of Random Data*, 3rd ed., John Wiley, Hoboken, N.J.
- Cannat, M., D. Sauter, V. Mendel, E. Ruellan, K. Okino, J. Escartin, V. Combiar, and M. Baala (2006), Modes of seafloor generation at a melt-poor ultraslow-spreading ridge, *Geology*, 34(7), 605–608, doi:10.1130/G22486.1.
- Canuto, V. M., A. Howard, Y. Cheng, and R. L. Miller (2004), Latitude-dependent vertical mixing and the tropical thermocline in a global OGCM, *Geophys. Res. Lett.*, 31, L16305, doi:10.1029/2004GL019891.
- Carbotte, S. M., et al. (2004), New integrated data management system for Ridge2000 and MARGINS research, *Eos Trans. AGU*, 85(51), 553, doi:10.1029/2004EO510002.
- Conkright, M. E., et al. (2007), *World Ocean Atlas 2001*, http://www.nodc.noaa.gov/OC5/WOA01/pr_woa01.html, Natl. Oceanogr. Data Cent., Silver Spring, Md., 2 Jan.
- Dillon, T. M. (1982), Vertical overturns: A comparison of Thorpe and Ozmidov length scales, *J. Geophys. Res.*, 87(C12), 9601–9613, doi:10.1029/JC087iC12p09601.
- Egbert, G. D., and R. D. Ray (2000), Significant dissipation of tidal energy in the deep ocean inferred from satellite altimeter data, *Nature*, 405(6788), 775–778, doi:10.1038/35015531.
- Egbert, G. D., and R. D. Ray (2001), Estimates of M2 tidal energy dissipation from TOPEX/POSEIDON altimeter data, *J. Geophys. Res.*, 106(C10), 22,475–22,502, doi:10.1029/2000JC000699.
- Egbert, G. D., and R. D. Ray (2003), Semi-diurnal and diurnal tidal dissipation from TOPEX/POSEIDON altimetry, *Geophys. Res. Lett.*, 30(17), 1907, doi:10.1029/2003GL017676.
- Freilich, M. H. (1997), Validation of vector magnitude datasets: Effects of random component errors, *J. Atmos. Oceanic Technol.*, 14(3), 695–703, doi:10.1175/1520-0426(1997)014<0695:VOVMDE>2.0.CO;2.
- Garrett, C., and E. Kunze (2007), Internal tide generation in the deep ocean, *Annu. Rev. Fluid Mech.*, 39, 57–87, doi:10.1146/annurev.fluid.39.050905.110227.
- Gille, S. T., M. M. Yale, and D. T. Sandwell (2000), Global correlation of mesoscale ocean variability with seafloor roughness from satellite altimetry, *Geophys. Res. Lett.*, 27(9), 1251–1254, doi:10.1029/1999GL007003.
- Goff, J. A. (1991), A global and regional stochastic analysis of near-ridge abyssal hill morphology, *J. Geophys. Res.*, 96(B13), 21,713–21,737, doi:10.1029/91JB02275.
- Goff, J. A., and T. H. Jordan (1989), Stochastic modeling of seafloor morphology: A parameterized Gaussian model, *Geophys. Res. Lett.*, 16(1), 45–48, doi:10.1029/GL016i001p00045.
- Goff, J. A., and W. H. F. Smith (2003), A correspondence of altimetric gravity texture to abyssal hill morphology along the flanks of the Southeast Indian Ridge, *Geophys. Res. Lett.*, 30(24), 2269, doi:10.1029/2003GL018913.
- Goff, J. A., W. H. F. Smith, and K. M. Marks (2004), The contributions of abyssal hill morphology and noise to altimetric gravity fabric, *Oceanography*, 17(1), 24–37.
- Jayne, S. R., and L. C. St Laurent (2001), Parameterizing tidal dissipation over rough topography, *Geophys. Res. Lett.*, 28(5), 811–814, doi:10.1029/2000GL012044.
- Kantha, L. H. (1995), Barotropic tides in the global oceans from a nonlinear tidal model assimilating altimetric tides: 1. Model description and results, *J. Geophys. Res.*, 100(C12), 25,283–25,308, doi:10.1029/95JC02578.
- Knauss, J. A. (1997), *Introduction to Physical Oceanography*, 2nd ed., 309 pp., Prentice Hall, Upper Saddle River, N. J.
- Kunze, E., and S. G. Llewellyn Smith (2004), The role of small-scale topography in turbulent mixing of the global ocean, *Oceanography*, 17(1), 55–64.
- Laws, E. (1997), *Mathematical Methods for Oceanographers: An Introduction*, 343 pp., John Wiley, Hoboken, N. J.
- Ledwell, J. R., E. T. Montgomery, K. L. Polzin, L. C. St. Laurent, R. W. Schmitt, and J. M. Toole (2000), Evidence for enhanced mixing over rough topography in the abyssal ocean, *Nature*, 403(6766), 179–182, doi:10.1038/35003164.
- Llewellyn Smith, S. G., and W. R. Young (2002), Conversion of the barotropic tide, *J. Phys. Oceanogr.*, 32(5), 1554–1566, doi:10.1175/1520-0485(2002)032<1554:COTBT>2.0.CO;2.
- Lonsdale, P. (1977), Deep-tow observations at Mounds Abyssal Hydrothermal Field, Galapagos Rift, *Earth Planet. Sci. Lett.*, 36(1), 92–110, doi:10.1016/0012-821X(77)90191-1.
- Macdonald, K. C. (1982), Mid-ocean ridges: Fine scale tectonic, volcanic and hydrothermal processes within the plate boundary zone, *Annu. Rev. Earth Planet. Sci.*, 10, 155–190, doi:10.1146/annurev.ea.10.050182.001103.
- Macdonald, K. C., and B. P. Luyendyk (1985), Investigation of faulting and abyssal hill formation on the flanks of the East Pacific Rise (21°N) using Alvin, *Mar. Geophys. Res.*, 7(4), 515–535, doi:10.1007/BF00368953.
- Macdonald, K. C., P. J. Fox, L. J. Perram, M. F. Eisen, R. M. Haymon, S. P. Miller, S. M. Carbotte, M.-H. Cormier, and A. N. Shor (1988), A new view of the mid-ocean ridge from the behavior of ridge-axis discontinuities, *Nature*, 335(6187), 217–225, doi:10.1038/335217a0.
- Macdonald, K. C., P. J. Fox, R. T. Alexander, R. Pockalny, and P. Gente (1996), Volcanic growth faults and the origin of Pacific abyssal hills, *Nature*, 380(6570), 125–129, doi:10.1038/380125a0.
- MathWorks (2007), MATLAB, software, Natick, Mass.
- Menard, H. W. (1967), Sea floor spreading topography and second layer, *Science*, 157(3791), 923–924, doi:10.1126/science.157.3791.923.
- Morgan, P., and L. Pender (2003), SEAWATER: A library of MATLAB computational routines for the properties of seawater, report, CSIRO Div. of Mar. Res., Melbourne, Victoria, Australia.
- Munk, W. (1966), Abyssal recipes, *Deep Sea Res. Part I*, 13, 707–730.
- Munk, W., and C. Wunsch (1998), Abyssal recipes II: Energetics of tidal and wind mixing, *Deep Sea Res., Part I*, 45, 1977–2010, doi:10.1016/S0967-0637(98)00070-3.
- Nash, J. D., M. H. Alford, E. Kunze, K. Martini, and S. Kelly (2007), Hotspots of deep ocean mixing on the Oregon continental slope, *Geophys. Res. Lett.*, 34, L01605, doi:10.1029/2006GL028170.
- National Geophysical Data Center (2006), GEODAS search criteria selection, http://ftp.ngdc.noaa.gov/mgg/gdas/gd_cri.html, Boulder, Colo., 2 Jan.
- Osborn, T. R. (1980), Estimates of the local-rate of vertical diffusion from dissipation measurements, *J. Phys. Oceanogr.*, 10(1), 83–89, doi:10.1175/1520-0485(1980)010<0083:EOTLRO>2.0.CO;2.
- Osborn, T. R., and C. S. Cox (1972), Oceanic fine structure, *Geophys. Fluid Dyn.*, 3, 321–345, doi:10.1080/03091927208236085.
- Polzin, K. L., J. M. Toole, J. R. Ledwell, and R. W. Schmitt (1997), Spatial variability of turbulent mixing in the abyssal ocean, *Science*, 276(5309), 93–96, doi:10.1126/science.276.5309.93.
- Small, C., and D. T. Sandwell (1992), An analysis of ridge axis gravity roughness and spreading rate, *J. Geophys. Res.*, 97(B3), 3235–3245, doi:10.1029/91JB02465.
- Smith, W. H. F. (1993), On the accuracy of digital bathymetric data, *J. Geophys. Res.*, 98(B6), 9591–9603, doi:10.1029/93JB00716.
- Smith, W. H. F. (1998), Seafloor tectonic fabric from satellite altimetry, *Annu. Rev. Earth Planet. Sci.*, 26, 697–747, doi:10.1146/annurev.earth.26.1.697.
- Smith, W. H. F., and D. T. Sandwell (1997), Global sea floor topography from satellite altimetry and ship depth soundings, *Science*, 277(5334), 1956–1962, doi:10.1126/science.277.5334.1956.
- Smith, W. H. F., and D. T. Sandwell (2004), Conventional bathymetry, bathymetry from space, and geodetic altimetry, *Oceanography*, 17(1), 8–23.
- St. Laurent, L., and C. Garrett (2002), The role of internal tides in mixing the deep ocean, *J. Phys. Oceanogr.*, 32(10), 2882–2899, doi:10.1175/1520-0485(2002)032<2882:TROI>2.0.CO;2.
- Toole, J. M., R. W. Schmitt, K. L. Polzin, and E. Kunze (1997), Near-boundary mixing above the flanks of a midlatitude seamount, *J. Geophys. Res.*, 102(C1), 947–959, doi:10.1029/96JC03160.
- Wessel, P., and W. H. F. Smith (1995), New version of the generic mapping tools released, *Eos Trans. AGU*, 79(47), 579, doi:10.1029/95EO00216.

J. J. Becker and D. T. Sandwell, Institute of Geophysics and Planetary Physics, Scripps Institution of Oceanography, 8795 Biological Grade, Room 1102, La Jolla, CA 92037, USA. (jj@becker.com)